Real-time evolution of static electron-phonon models in time-dependent electric fields

Manuel Weber ●[1,2] and James K. Freericks ●[1]

[1]*Department of Physics, Georgetown University, Washington, DC 20057, USA*
[2]*Max-Planck-Institut für Physik komplexer Systeme, Nöthnitzer Str. 38, 01187 Dresden, Germany*

We present an exact Monte Carlo method to simulate the nonequilibrium dynamics of electron-phonon models in the adiabatic limit of zero phonon frequency. The classical nature of the phonons allows us to sample the equilibrium phonon distribution and efficiently evolve the electronic subsystem in a time-dependent electromagnetic field for each phonon configuration. We demonstrate that our approach is particularly useful for charge-density-wave systems experiencing pulsed electric fields, as they appear in pump-probe experiments. For the half-filled Holstein model in one and two dimensions, we calculate the out-of-equilibrium response of the current and the energy after a pulse is applied as well as the photoemission spectrum before and after the pump. Finite-size effects are under control for chains of 162 sites (in one dimension) or 16×16 square lattices (in two dimensions).

I. INTRODUCTION

Electron-phonon interaction plays an important role in strongly correlated materials in which it can give rise to superconductivity, the formation of polarons, or charge-density-wave (CDW) order. Progress in ultrafast optical spectroscopy has opened up a path to drive these materials out of equilibrium using strong light pulses and probe the evolution of these phases or the emergence of new phenomena directly in the real-time domain [1]. A recent focus of pump-probe experiments has been on CDW materials like TaS_2 [2–8] or the rare-earth tri-tellurides [9,10]. Pumping light into these materials can lead to a long-time ringing of the CDW amplitude mode, as observed in angle-resolved photoemission [2], and even to long-lived metastable phases showing a large change in conductivity [4]. While it is widely debated whether in these materials CDW order arises from the Peierls instability or from a purely electronic mechanism, phonons always play an important role in the out-of-equilibrium dynamics and relaxation toward a steady state.

Theoretical modeling of these systems is often based on time-dependent Ginzburg-Landau theory or Boltzmann equations, which provide a phenomenological description of the CDW state. Migdal-Eliashberg theory is very successful for phonon-mediated superconductors but less reliable for CDW systems (because of the different ways these systems are screened). To understand the microscopic details of these systems, we need efficient numerical techniques to solve the quantum many-particle problem out of equilibrium. While for a realistic modeling we have to consider both electron-electron and electron-phonon interactions, the exact solution of the phonon part turns out to be the biggest challenge for simulations. For small clusters, exact diagonalization has been performed with classical [11,12] and quantum phonons [13]. The density-matrix renormalization group (DMRG) has been applied to one-dimensional (1D) systems [14–17], but so far simulations could only reach short timescales on small lattices. The major challenge for wave-function-based methods is the growing number of excited phonons with time. Already in thermal equilibrium, the unbound bosonic Hilbert space makes these methods less efficient than for purely electronic systems. Quantum Monte Carlo methods can avoid this problem and recently made progress in determining the equilibrium phase diagrams of phonon-coupled systems in higher dimensions using exact [18–28] and variational [29,30] approaches, but the dynamical sign problem prevents applications to the real-time domain. In infinite dimensions, nonequilibrium dynamical mean-field theory [31,32] gives exact results for the CDW phase in the purely electronic Falicov-Kimball model [33–35], whereas phonons can only be included approximately using a strong-coupling impurity solver [36,37] or Migdal's approximation [38]. Approximate results can also be obtained from weak-coupling perturbation theory [39–41]. At this time, all available methods that solve the nonequilibrium electron-phonon problem exactly are restricted to small system sizes and short timescales, inhibiting simulations for the experimentally relevant case of quasi-2D systems.

In this article, we show that the electron-phonon problem driven by a time-dependent electromagnetic field can be solved efficiently in the adiabatic limit of infinite ion mass. In this limit, the phonon frequency is zero and the lattice loses its dynamics. As a result, the phonons become classical variables and their thermal distribution function can be sampled using

a classical Monte Carlo method in combination with exact diagonalization of a quadratic electronic Hamiltonian [42,43]. A similar approach had been applied to the double-exchange model for the manganites where electrons couple to classical spins [44]. While previous work mainly concentrated on equilibrium properties, we show that this class of models is well suited to study the response of a minimal interacting system to a pulsed electric field as it appears in pump-probe scenarios. Because for each phonon configuration the full problem reduces to a noninteracting system in a time-dependent field, the time evolution can be obtained by iteratively diagonalizing the time-dependent Hamiltonian. Using the example of the Holstein model, we demonstrate that our approach can access timescales that are long enough to reach a steady state after a pulsed electric field has been applied. System sizes of 162 sites for a 1D chain and 16×16 sites for a 2D square lattice are sufficient to control finite-size effects. Starting from different initial temperatures, we show results for time-dependent observables like current and energy as a pump field is applied, as well as the photoemission spectra before and after the pump.

The adiabatic approximation of zero phonon frequency is often used for modeling the equilibrium properties of CDW materials. In many of these materials, the phonon mode that drives the Peierls instability went soft, so it only has a few meV [45] in the ordered phase, which is much smaller than the electronic energy scale, and the adiabatic approximation turns out to be in good agreement with experiments [46]. Indeed, a classical treatment of the phonons is justified as long as the Peierls gap and/or the temperature are larger than the phonon frequency [47], which was recently confirmed by quantum Monte Carlo simulations [48]. The application of strong electric fields in pump-probe experiments raises the average energy of the system to be much higher than the phonon frequencies, implying that the adiabatic approximation should be accurate for pumped CDW systems at short timescales. Our results in the adiabatic limit capture the relaxation of the electronic subsystem from scattering off the phonons after a pump was applied. However, the adiabatic approximation will not be able to describe the correct long-time behavior of real materials, as the phonons are conserved quantities and cannot exchange energy with the electronic subsystem. At the end of this article, we will discuss how this limitation can be overcome by including a classical dynamics for the phonons.

The paper is organized as follows. In Sec. II we define the Holstein model in a time-dependent electric field, in Sec. III we introduce the equilibrium and nonequilibrium formalism of the Monte Carlo method, in Sec. IV we present results for the 1D and 2D Holstein model, and in Sec. V we conclude.

II. MODEL

The Holstein model [49] is given by the Hamiltonian

$$\hat{H} = -J \sum_{\langle i,j \rangle \sigma} \hat{c}_{i\sigma}^{\dagger} \hat{c}_{j\sigma} + \sum_{i} \left(\frac{K}{2} \hat{Q}_i^2 + \frac{1}{2M} \hat{P}_i^2 \right)$$
$$+ g \sum_{i\sigma} \hat{Q}_i \left(\hat{n}_{i\sigma} - \frac{1}{2} \right). \tag{1}$$

The first term describes the nearest-neighbor hopping of electrons with amplitude J. Here, $\hat{c}_{i\sigma}^{\dagger}$ ($\hat{c}_{i\sigma}$) creates (annihilates) an electron at site i with spin σ. The second term represents local harmonic oscillators with displacement operators $\hat{Q}_i$ and momenta $\hat{P}_i$. We define the optical phonon frequency $\omega_0 = \sqrt{K/M}$, where K is the stiffness constant and M is the phonon mass. The third term couples the phonon displacement $\hat{Q}_i$ to the local electron density $\hat{n}_{i\sigma} = \hat{c}_{i\sigma}^{\dagger} \hat{c}_{i\sigma}$ via a constant g. We use the dimensionless coupling parameter $\lambda = g^2/KW$, where W is the bandwidth of the noninteracting electron system. We have $W = 4J$ for the 1D chain and $W = 8J$ for the 2D square lattice. We use $J = 1$ as the unit of energy and consider half-filling with $\langle \hat{n}_{i\sigma} \rangle = 1/2$.

In the following, we only consider the adiabatic limit $M \to \infty$, which corresponds to $\omega_0 \to 0$ at fixed $K = M\omega_0^2$. Then, the phonon momenta $\hat{P}_i$ drop out of the Hamiltonian, and the displacement operators $\hat{Q}_i$ can be replaced by classical variables q_i. The ground state of the adiabatic Holstein model can be obtained from the variational principle. At half-filling, the ground-state energy $E(\vec{q})$ for the 1D chain and for the 2D square lattice considered in this article is minimized by the mean-field ansatz $q_i = \Delta/g \cos(\mathbf{K} \cdot \mathbf{R}_i)$. The periodic lattice distortion is accompanied by CDW order with ordering vector $\mathbf{K} = \pi$ [$\mathbf{K} = (\pi, \pi)$] for the 1D (2D) case, which corresponds to an alternating (checkerboard) pattern of the electronic density. The single-particle gap Δ can be estimated self-consistently from the mean-field equations. For any finite electron-phonon coupling λ we get $\Delta > 0$ and the ground state is twofold degenerate under $\Delta \to -\Delta$. At zero temperature, the perfect dimerization reduces the Holstein model to a single-particle Hamiltonian with a fully occupied lower band and an empty upper band separated by the gap Δ. At finite temperatures, the adiabatic Holstein model remains an interacting problem that can be solved with the Monte Carlo method discussed in Sec. III. In 1D, long-range CDW order can only exist at zero temperature due to the spontaneous breaking of a discrete $\mathbb{Z}_2$ lattice symmetry, so that any finite temperature leads to a disordered phase. However, the Peierls gap Δ is only fully filled in at a finite coherence temperature where short-range CDW correlations disappear [50]. On the square lattice, CDW order remains stable up to a critical temperature, above which one can find a disordered phase [18]. In both cases, CDW order is strongest at $\omega_0 = 0$. While the CDW ground state of the 1D chain can be destroyed at a critical $\omega_{0,c}$, it is expected to remain stable for the 2D square lattice [18]. For further information on the effects of quantum lattice fluctuations on the thermodynamic properties of the Holstein model, we refer to Refs. [18,48].

After preparing the Holstein model in a thermal state, we want to drive the system out of equilibrium using a time-dependent classical electromagnetic field

$$\mathbf{E}(\mathbf{r}, t) = -\nabla \Phi(\mathbf{r}, t) - \frac{1}{c} \frac{\partial \mathbf{A}(\mathbf{r}, t)}{\partial t}, \tag{2}$$

$$\mathbf{B}(\mathbf{r}, t) = \nabla \times \mathbf{A}(\mathbf{r}, t). \tag{3}$$

The electric field $\mathbf{E}(\mathbf{r}, t)$ and the magnetic field $\mathbf{B}(\mathbf{r}, t)$ can be represented in terms of the static potential $\Phi(\mathbf{r}, t)$ and the vector potential $\mathbf{A}(\mathbf{r}, t)$. We use the temporal gauge with $\Phi(\mathbf{r}, t) = 0$. Then, the vector potential can be included in

Eq. (1) via the Peierls substitution

$$\hat{c}_{i\sigma}^{\dagger}\hat{c}_{j\sigma} \rightarrow \exp\left[-\frac{ie}{\hbar c}\int_{\mathbf{R}_i}^{\mathbf{R}_j}\mathbf{A}(\mathbf{r},t)\,d\mathbf{r}\right]\hat{c}_{i\sigma}^{\dagger}\hat{c}_{j\sigma}. \qquad (4)$$

Here, $\mathbf{R}_i$ is the Bravais vector that points toward lattice site i. In the following, we set $e = \hbar = c = 1$. We pump our system with a spatially homogeneous but time-dependent electric field

$$\mathbf{E}(t) = \mathbf{E}_0 \exp\left(-\frac{t^2}{2\sigma_{\mathrm{p}}^2}\right)\sin(\omega_{\mathrm{p}}t). \qquad (5)$$

Here, $\mathbf{E}_0$ is the field amplitude, σ_{p} is the pump width, and ω_{p} is the pump frequency. We assume that the pump pulse is centered at $t = 0$, and we choose a field that has no dc component, consistent with optical pulse excitation. Our approach neglects some magnetic field effects generated near when the field is turned on and turned off, because this field does not satisfy Maxwell's equations. This approximation corresponds to describing optical light in a crystal as having vanishing momentum, which is a common approximation.

III. METHOD

Microscopic models of electrons that only interact with classical degrees of freedom can be solved efficiently using the Monte Carlo method of Ref. [51]. The method has been applied to a variety of scenarios, including the coupling to adiabatic phonons in Holstein or Su-Schrieffer-Heeger models [42,43], localized electrons in the Falicov-Kimball model [52], classical spins in double-exchange models [44], or $\mathbb{Z}_2$ spins in effective models for Kitaev spin liquids [53].

In the following, we first review the equilibrium formulation of the Monte Carlo method before we discuss the nonequilibrium formalism.

A. Equilibrium formalism

The Monte Carlo method described in this section applies to a generic Hamiltonian of the form

$$\hat{H} = \hat{H}_{\mathrm{el}}(\vec{q}) + V(\vec{q}) \qquad (6)$$

that can be split into a classical potential $V(\vec{q})$ and a bilinear electronic part

$$\hat{H}_{\mathrm{el}}(\vec{q}) = \sum_{ij}\sum_{\sigma}\hat{c}_{i\sigma}^{\dagger}\,\mathcal{H}_{ij}(\vec{q})\,\hat{c}_{j\sigma} \qquad (7)$$

coupled to classical degrees of freedom $\vec{q}$. For simplicity of notation, we assume that the single-particle Hamiltonian $\hat{\mathcal{H}}(\vec{q})$ is equal for all spin components. The partition function of Hamiltonian (6) takes the form

$$Z = \int d\vec{q}\, e^{-\beta V(\vec{q})}Z_{\mathrm{el}}[\vec{q}], \qquad (8)$$

where $Z_{\mathrm{el}}[\vec{q}] = \mathrm{Tr}\exp[-\beta(\hat{H}_{\mathrm{el}}(\vec{q}) - \mu\hat{N})]$ is the grand-canonical partition function of the electronic subsystem (for a specific configuration $\vec{q}$ of the classical variables), $\beta = 1/k_{\mathrm{B}}T$ is the inverse temperature, μ is the chemical potential, and $\hat{N}$ is the total particle-number operator.

Any expectation value of the full system,

$$\langle\hat{O}\rangle = \int d\vec{q}\, W_{\mathrm{eq}}[\vec{q}]\,\langle\!\langle\hat{O}\rangle\!\rangle_{\vec{q}}, \qquad (9)$$

can be expressed as a weighted average over the equilibrium distribution of classical variables $\vec{q}$,

$$W_{\mathrm{eq}}[\vec{q}] = \frac{1}{Z}e^{-\beta V(\vec{q})}Z_{\mathrm{el}}[\vec{q}], \qquad (10)$$

and the noninteracting expectation value of the electronic subsystem for a fixed configuration $\vec{q}$,

$$\langle\!\langle\hat{O}\rangle\!\rangle_{\vec{q}} = \frac{1}{Z_{\mathrm{el}}[\vec{q}]}\mathrm{Tr}\left\{e^{-\beta[\hat{H}_{\mathrm{el}}(\vec{q})-\mu\hat{N}]}\,\hat{O}_{\vec{q}}\right\}. \qquad (11)$$

The classical variables $\vec{q}$ can be sampled from $W_{\mathrm{eq}}[\vec{q}]$ using the Metropolis-Hastings algorithm. We propose local updates $q_i \rightarrow q_i' = q_i + \Delta q$ which only change a single coordinate. For each Monte Carlo update, we need to diagonalize $\hat{\mathcal{H}}(\vec{q})$ to obtain

$$\hat{H}_{\mathrm{el}}(\vec{q}) = \sum_{\alpha\sigma}\epsilon_{\alpha}\hat{\gamma}_{\alpha\sigma}^{\dagger}\hat{\gamma}_{\alpha\sigma}, \quad \hat{c}_{i\sigma} = \sum_{\alpha}\Gamma_{i\alpha}\hat{\gamma}_{\alpha\sigma}. \qquad (12)$$

Here, $\Gamma_{i\alpha}$ is the transformation matrix from real-space coordinates to the energy eigenbasis with eigenvalues ϵ_{α}. Unless necessary, we will suppress the $\vec{q}$ dependence of the eigenbasis in the following. With this, the Monte Carlo weight

$$W_{\mathrm{eq}}[\vec{q}] = \frac{1}{Z}e^{-\beta V(\vec{q})}\prod_{\alpha\sigma}\left\{1 + e^{-\beta(\epsilon_{\alpha}[\vec{q}]-\mu)}\right\} \qquad (13)$$

is always positive and the Metropolis acceptance probability becomes $R(\vec{q} \rightarrow \vec{q}') = \min(1, W_{\mathrm{eq}}[\vec{q}']/W_{\mathrm{eq}}[\vec{q}])$. To obtain independent configurations, we need to perform $O(L)$ local updates. Therefore, the algorithm scales as $O(L^4)$. To improve the sampling at low temperatures, we use an exchange Monte Carlo technique [54]. For further details on our implementation, see Ref. [50].

For each Monte Carlo configuration $\vec{q}$, observables are calculated from Eq. (11). Because expectation values are taken with respect to a quadratic Hamiltonian, Wick's theorem is valid for each $\vec{q}$. Therefore, the computation of thermal averages only requires access to the equilibrium density matrix

$$\langle\!\langle\hat{c}_{i\sigma}^{\dagger}\hat{c}_{j\sigma}\rangle\!\rangle_{\vec{q}} = \sum_{\alpha}\Gamma_{j\alpha}\,n_{\mathrm{F}}(\epsilon_{\alpha})\,\Gamma_{\alpha i}^{\dagger}. \qquad (14)$$

Here, $n_{\mathrm{F}}(\epsilon_{\alpha}) = 1/\{1 + \exp[-\beta(\epsilon_{\alpha} - \mu)]\}$ is the Fermi-Dirac distribution.

B. Nonequilibrium formalism

The calculation of observables from Eq. (11) is not restricted to the equilibrium case. Wick's theorem remains valid in the real-time domain so that any time-dependent correlation function can be obtained from the greater and lesser Green's functions,

$$i\,G_{ij\sigma}^{>}(t,t';\vec{q}) = \langle\!\langle\hat{c}_{i\sigma}(t)\,\hat{c}_{j\sigma}^{\dagger}(t')\rangle\!\rangle_{\vec{q}}, \qquad (15)$$

$$-i\,G_{ij\sigma}^{<}(t,t';\vec{q}) = \langle\!\langle\hat{c}_{j\sigma}^{\dagger}(t')\,\hat{c}_{i\sigma}(t)\rangle\!\rangle_{\vec{q}}. \qquad (16)$$

The time-dependent single-particle operators are defined in the Heisenberg picture,

$$\hat{c}_{i\sigma}(t) = \hat{U}^\dagger(t, t_0) \, \hat{c}_{i\sigma}(t_0) \, \hat{U}(t, t_0), \qquad (17)$$

and the time-evolution operator from t_0 to t is given by

$$\hat{U}(t, t_0) = \hat{\mathcal{T}}_t \, \exp\left[-i \int_{t_0}^{t} dt' \hat{H}(t') \right], \qquad (18)$$

where $\hat{\mathcal{T}}_t$ is the time-ordering operator. To get access to $\hat{U}(t, t_0)$, we discretize the real-time evolution into small intervals Δt, so that $\hat{U}(t, t_0)$ can be obtained sequentially via

$$\hat{U}(t, t_0) = \hat{U}(t, t - \Delta t) \, \hat{U}(t - \Delta t, t_0). \qquad (19)$$

Then, the time-evolution operator for a single time step can be approximated as

$$\hat{U}(t, t - \Delta t) = \exp[-i\Delta t \, \hat{H}(t)] + O(\Delta t^2). \qquad (20)$$

Here, we choose $\hat{H}(t)$ to be constant for the time step Δt. We want to emphasize that the time evolution with Eq. (20) is still exact if $\hat{H}(t)$ has a discretized time dependence. Because the Hamiltonian is quadratic, the time evolution of the annihilation operator,

$$\hat{c}_{i\sigma}(t) = \sum_j \mathcal{U}_{ij}(t, t - \Delta t) \, \hat{c}_{j\sigma}(t - \Delta t), \qquad (21)$$

is determined by the single-particle evolution operator. Equation (21) can be derived from the Heisenberg equation of motion, $i \, d\hat{c}_{i\sigma}(t)/dt = [\hat{c}_{i\sigma}(t), \hat{H}(t)]$, using Eqs. (17) and (20). We obtain

$$\mathcal{U}_{ij}(t, t - \Delta t) = \sum_\alpha \Gamma_{i\alpha}(t) \, e^{-i\Delta t \, \epsilon_\alpha(t)} \, \Gamma_{\alpha j}^\dagger(t), \qquad (22)$$

which can be calculated by diagonalizing $\hat{\mathcal{H}}(\vec{q}, t)$ according to Eq. (12). After plugging Eq. (21) into Eqs. (15) and (16), the greater and lesser Green's functions eventually become

$$i \, G_{ij\sigma}^>(t, t'; \vec{q}) = \sum_\alpha \mathcal{U}_{i\alpha}(t, t_0) \, [1 - n_F(\epsilon_\alpha)] \, \mathcal{U}_{\alpha j}^\dagger(t', t_0),$$

$$-i \, G_{ij\sigma}^<(t, t'; \vec{q}) = \sum_\alpha \mathcal{U}_{i\alpha}(t, t_0) \, n_F(\epsilon_\alpha) \, \mathcal{U}_{\alpha j}^\dagger(t', t_0), \qquad (23)$$

where $\mathcal{U}_{i\alpha}(t, t_0) = \sum_j \mathcal{U}_{ij}(t, t_0) \, \Gamma_{j\alpha}(t_0)$. We assumed that at the initial time t_0 the system is in thermal equilibrium, and therefore we used Eq. (14) to include $n_F(\epsilon_\alpha)$ in Eq. (23).

The computational effort for calculating observables in the real-time domain depends strongly on the scenario for the time evolution. The simplest case corresponds to a time-independent Hamiltonian where the evolution operator $\mathcal{U}_{\alpha\alpha}(t, t_0) = \exp[-i(t - t_0)\epsilon_\alpha]$ is fully determined by the equilibrium eigenvalues. As a result, one can obtain the equilibrium spectral functions for each Monte Carlo configuration directly from the Lehmann representation. This approach can also be combined with nonequilibrium Green's function techniques, e.g., to calculate the charge transport through the system when noninteracting leads are attached [55]. Another simple scenario involves parameter quenches where the Hamiltonian has to be diagonalized once before and once after the quench but eigenvalues are constant within each time domain [56]. For a more generic time-evolution scenario, $\hat{\mathcal{H}}(t)$

has to be diagonalized for each step Δt such that the computational effort for each measurement becomes $O(L^3 N_t)$, where N_t is the number of time steps. Evolving the system up to long timescales will quickly dominate the computational costs over the sampling of the equilibrium distribution. In this article, we demonstrate that the Monte Carlo method introduced above is nonetheless very powerful for the time evolution with pulsed electric fields. Further simplifications can occur for periodic driving where Floquet theory applies [57].

C. Calculation of observables

Any time-dependent single-particle observable can be calculated from the greater and lesser Green's functions in Eq. (23). We prepare our system at an initial time t_0 in the equilibrium eigenbasis labeled by the index α. The time dependence of Eq. (23) can then be accessed by propagating $\mathcal{U}_{i\alpha}(t, t_0)$ forward in time. For this, we iteratively diagonalize $\hat{\mathcal{H}}(t)$, set up the evolution operator for a time step Δt according to Eq. (22), and carry out the time evolution in Eq. (19) via a matrix multiplication.

Equal-time observables can be calculated after each time step from $G_{ij\sigma}^<(t, t)$. In this article, we will consider the electronic energy

$$E_{\text{el}}(t) = -\frac{J}{L} \sum_{i\sigma} \left\langle e^{-i\phi_{i\ell}(t)} \hat{c}_{\mathbf{R}_i, \sigma}^\dagger(t) \, \hat{c}_{\mathbf{R}_i + \mathbf{e}_\ell, \sigma}(t) + \text{H.c.} \right\rangle \quad (24)$$

as well as the total current $j(t) = \mathbf{j}(t) \cdot \mathbf{E}_0 / |\mathbf{E}_0|$, where

$$j_\ell(t) = -\frac{J}{L} \sum_{i\sigma} \left\langle i \, e^{-i\phi_{i\ell}(t)} \hat{c}_{\mathbf{R}_i, \sigma}^\dagger(t) \, \hat{c}_{\mathbf{R}_i + \mathbf{e}_\ell, \sigma}(t) + \text{H.c.} \right\rangle \quad (25)$$

is the component in the $\ell \in \{x, y\}$ direction, and $\mathbf{e}_\ell$ is the corresponding translation vector. Here, $\phi_{i\ell}(t)$ is the flux created by the site- and time-dependent vector potential in Eq. (4).

To get access to the full Green's functions, we tabulate $\mathcal{U}_{i\alpha}(t, t_0)$ for each time step and only evaluate Eq. (23) when the time evolution is completed. In this way, we can calculate the photoemission spectrum [58]

$$P(\omega, t_{\text{probe}}) \simeq -i \int_{-\infty}^{\infty} dt \int_{-\infty}^{\infty} dt' \, s(t) \, s(t') \, e^{-i\omega(t - t')}$$

$$\times \frac{1}{L} \sum_{i\sigma} G_{ii\sigma}^<(t, t') \qquad (26)$$

from the local lesser Green's function. We use a Gaussian envelope function for the probe pulse,

$$s(t) = \frac{1}{\sqrt{2\pi} \, \sigma_{\text{probe}}} \, \exp\left[-\frac{(t - t_{\text{probe}})^2}{2\sigma_{\text{probe}}^2} \right], \qquad (27)$$

centered at time t_{probe} and with width σ_{probe}. It is sufficient to evaluate $G_{ii\sigma}^<(t, t')$ for t, t' chosen from an interval around t_{probe} and in the end perform the discretized Fourier transform.

IV. RESULTS

A. Spinless Holstein model in 1D

We first consider the 1D spinless Holstein model as it has become the standard test case for numerical approaches to the electron-phonon problem. We set $\lambda = 0.5$ and restrict our
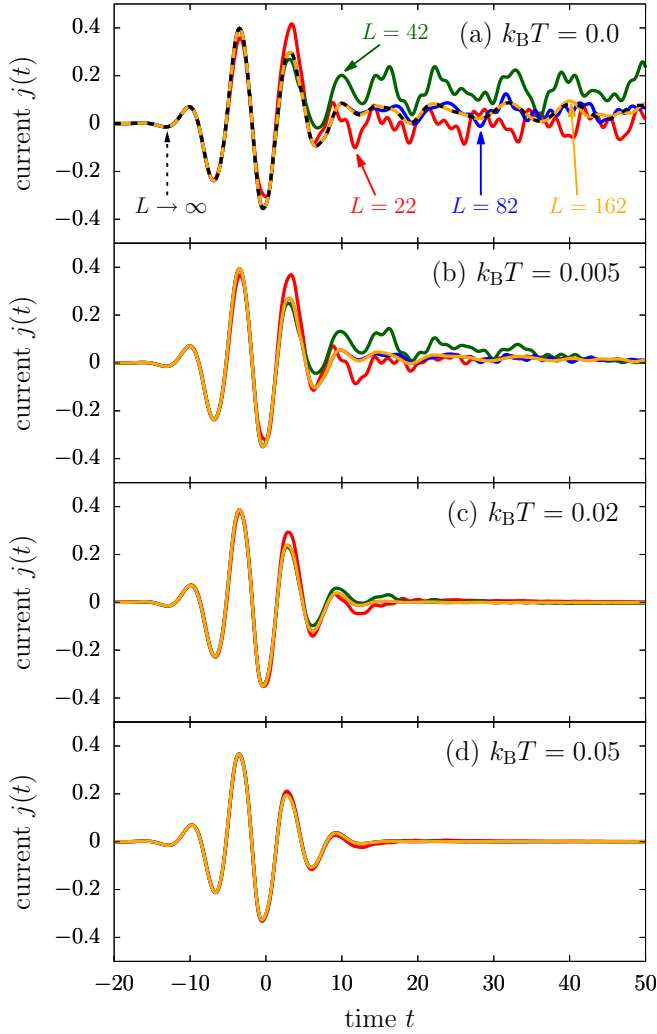
FIG. 1. Finite-size analysis of the current in the 1D spinless Holstein model for different initial temperatures. Here, $\lambda = 0.5$, $\Delta t = 0.1$. Error bars are smaller than the linewidth.
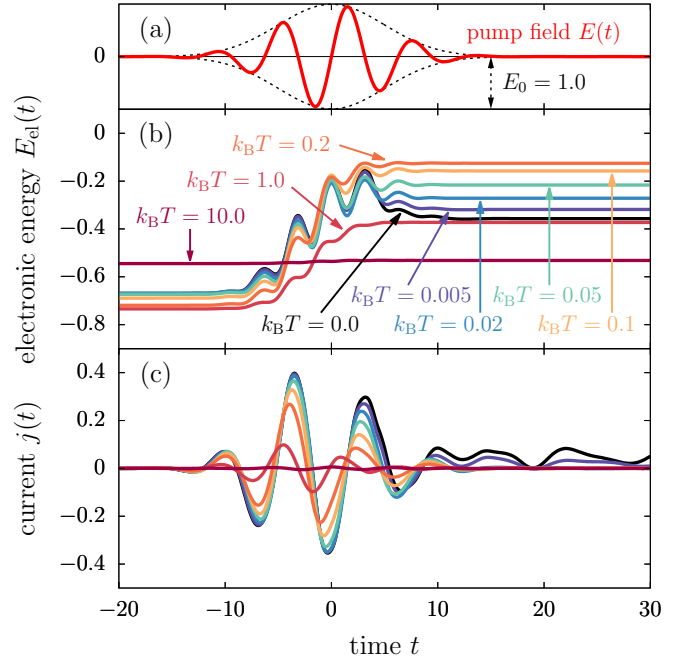

FIG. 2. Time-dependent response of the 1D spinless Holstein model for different initial temperatures. For the pump field shown in panel (a), we plot (b) the electronic energy and (c) the current. Here, $\lambda = 0.5$, $L = 162$, $\Delta t = 0.1$.

discussion to the half-filled case, for which the thermodynamic properties were studied in Ref. [50]. For the real-time evolution, we apply the pulsed electric field defined in Eq. (5) with $E_0 = 1.0$, $\sigma_p = 5.0$, and $\omega_p = 1.0$. We use time steps of $\Delta t = 0.1$ for which discretization effects are smaller than the linewidths in our plots [59].

Figure 1 shows a finite-size analysis of the current for different initial temperatures. The effect of finite lattices is strongest at $k_B T = 0$ in Fig. 1(a), where the Holstein model reduces to a noninteracting two-band problem via the perfect periodic lattice distortion $q_i = (-1)^i \Delta/g$. For $\lambda = 0.5$, we estimate the single-particle gap as $\Delta \approx 0.34$. At $k_B T = 0$, the real-time evolution of the two-band system can be calculated efficiently [60] such that we can get converged results in system size. Figure 1(a) shows that the onset of finite-size effects can be delayed to longer times with increasing L. For $L = 162$, the current is converged up to $t = 40$. Starting our simulations at finite temperatures substantially reduces finite-size effects, as demonstrated in Figs. 1(b)–1(d). The reduction of lattice-size effects coincides with the suppression of short-

range CDW correlations and the filling-in of the Peierls gap at $k_B T \approx 0.1$. For 1D systems, we also find that finite-size effects are stronger for pulsed electric fields than for the dc fields considered in Ref. [57].

In Fig. 2, we study the effect of the initial temperature on the electronic energy $E_{el}(t)$ and the current $j(t)$. We set $L = 162$ for which finite-size effects are negligible. We find that the oscillations of $E_{el}(t)$ in Fig. 2(b) closely follow the time dependence of the pump field in Fig. 2(a). In the low-temperature regime, the initial energy only changes slightly with increasing $k_B T$, whereas the final energy substantially increases with $k_B T$. It therefore appears that the heating induced by the pump is more effective in the presence of thermal fluctuations that have filled in the equilibrium Peierls gap. This is in contrast to the scenario of a constant applied field where E_{el} gets closest to an infinite-temperature steady state for the lowest $k_B T$ [57]. Only at the highest temperatures does the final energy decrease again. This is in agreement with the phonon-induced disorder becoming stronger at higher $k_B T$. Figure 2(c) shows that the current is increasingly damped with higher $k_B T$. In particular, for any $k_B T > 0$ the current approaches zero in the long-time limit.

Figure 3 shows the photoemission spectra $P(\omega)$ before and after the pump field is applied, as calculated from Eq. (26). We use a probe width of $\sigma_{probe} = 10.0$ to have high-energy resolution and set $t_{probe} = \pm 50.0$ for which the spectra have converged to their long-time limits $t \to \pm \infty$. Figure 3(a) shows $P(\omega)$ in the initial state for different temperatures. At $k_B T = 0$, $P(\omega)$ probes the occupation of the lower band in the density of states. Note that the square-root singularities at the band edges are smeared out by the finite probe width. Thermal fluctuations of the phonons lead to a broadening of the spectral
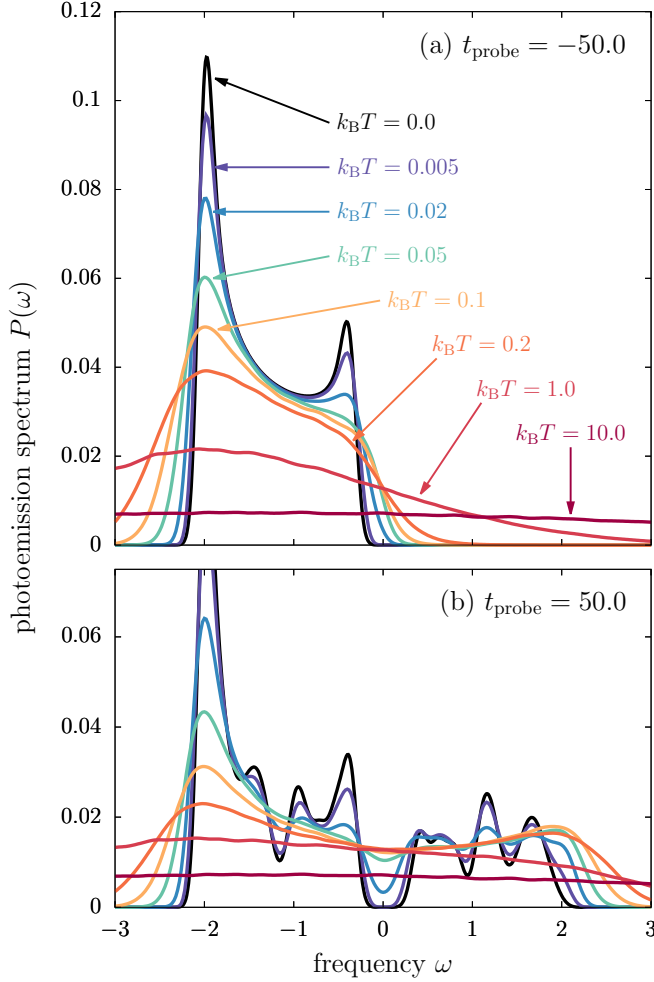
FIG. 3. Photoemission spectrum of the 1D spinless Holstein model (a) before and (b) after the pump for different initial temperatures. Here, $L = 162$, $\lambda = 0.5$, $\Delta t = 0.1$.

features and a closing of the single-particle gap [50]. Because $P(\omega)$ probes the occupation of all available states according to the Fermi-Dirac distribution, we find an exponentially activated tail of excitations for $\omega > 0$. After the pump has been applied, the photoemission spectrum in Fig. 3(b) includes substantial excitations in the upper band. Our exact approach allows us to resolve the fine structure of the excitation spectrum, which includes several peaks in the upper band. The main effect of the thermal fluctuations is the broadening of the sharp peaks that appear in the zero-temperature limit of perfect CDW order. Moreover, with increasing $k_B T$ the occupation of the highest accessible states at the upper band edge increases.

B. Spinful Holstein model in 2D

In the following, we apply our method to the 2D spinful Holstein model on the square lattice. At half-filling, the equilibrium problem has a thermal phase transition from a low-temperature CDW phase to a disordered phase that falls into the Ising universality class [18]. We consider $\lambda = 0.15$ for which the mean-field gap at $k_B T = 0$ is $\Delta \approx 0.55$ and the critical temperature is $k_B T_c \approx 0.1$ [18]. Starting from a

thermal state, we drive our system with the pulsed electric field of Eq. (5) applied in the diagonal direction $\mathbf{E}_0 = (1, 1)$ with $\sigma_p = 5.0$ and $\omega_p = 1.0$. We use $\Delta t = 0.1$.

We start our discussion of the 2D Holstein model with a finite-size analysis of our nonequilibrium observables. Similar to the 1D case, lattice-size effects are largest at $k_B T = 0$, where the half-filled Holstein model reduces to a noninteracting two-band problem. While thermal lattice fluctuations typically reduce lattice-size effects by broadening the δ excitations of a noninteracting system, tight-binding models on the square lattice usually suffer from strong size effects due to large level degeneracies. A common trick in equilibrium Monte Carlo simulations is to lift these degeneracies with a static magnetic field that vanishes for $L \to \infty$ [61]. Threading the entire lattice with one magnetic flux quantum leads to an improved scaling already for small L. Figure 4 compares the finite-size analysis of the current, electronic energy, and photoemission spectrum in the CDW phase at $k_B T = 0.05$ with and without an applied magnetic flux Φ. Our simulations reach $L \times L$ lattices with $L \leqslant 20$. For $\Phi = 0$, the current in Fig. 4(a) and the electronic energy in Fig. 4(b) show significant size effects at the longest times and even at intermediate times $t \approx 0$ they are not yet converged with L. By contrast, Figs. 4(d) and 4(e) show quick convergence at $t \approx 0$ for $\Phi = 1$. Moreover, $\Phi = 1$ suppresses the finite-size oscillations of the current at the longest times and leads to converged results for $L \simeq 20$. The presence of the flux cannot fully eliminate the size effects of the final electronic energy in Fig. 4(e), but it seems to enforce a monotonic dependence of $E_{el}(L)$. The photoemission spectra in Figs. 4(c) and 4(f) show the largest improvement when a flux is included. For $\Phi = 0$, only the Peierls gap and the bandwidth can be estimated reliably, whereas the remaining spectrum is dominated by broadened δ peaks which only slowly evolve into well-defined bands with increasing L. For $\Phi = 1$, a continuous spectrum that contains all the main features is already obtained for $L = 8$. The fine structure of the lower and upper bands can be clearly identified with increasing lattice sizes. All in all, the presence of a magnetic flux greatly reduces finite-size effects in our nonequilibrium observables and enables a reliable estimation of the photoemission spectra. Hence, we will use $\Phi = 1$ for all results discussed below.

Figure 5 shows $E_{el}(t)$ and $j(t)$ for different initial temperatures at $L = 16$. Our finite-size analysis suggests that the final energies in Fig. 5(b) might not be fully converged in L, but we expect the relative changes with $k_B T$ to be consistent. Similar to the 1D case, the final electronic energy increases with temperature up to $k_B T \approx 1.0$. Only for higher temperatures does the thermal phonon disorder reduce the energy absorption again. As long as the pump field is applied, the current in Fig. 5(c) remains rather stable against thermal fluctuations if the initial state was in the CDW phase. Moreover, the long-time tail at $k_B T = 0$ is only weakly damped by thermal fluctuations. For the longest times considered in Fig. 5(c), the damping towards zero current only becomes stronger as we approach $k_B T_c \approx 0.1$. If we initialize our system deep in the disordered phase, the current gets significantly damped also at intermediate times. Interestingly, we observe a slight enhancement of $j(t)$ at early times for $k_B T = 0.1$ and 0.2. This might be related to the finite signal in the zero-frequency
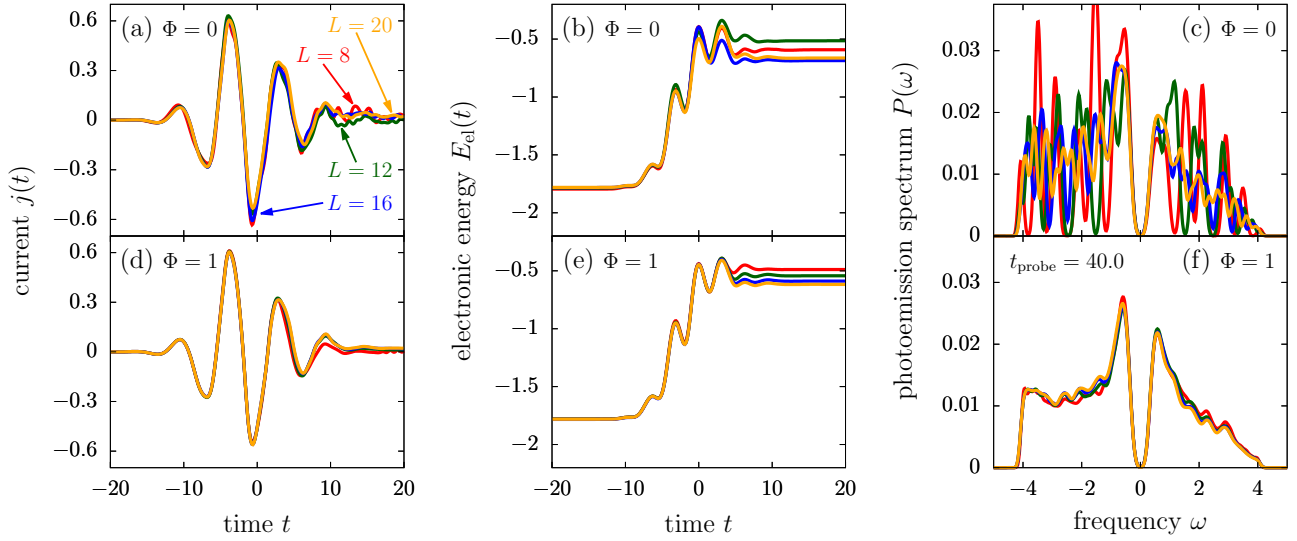
FIG. 4. Finite-size analysis of the current, electronic energy, and photoemission spectrum for the 2D spinful Holstein model on the square lattice. For each observable, we compare the size dependence of the plain system [(a)–(c)] with the situation where one magnetic flux quantum $\Phi = 1$ is threaded through the entire lattice [(d)–(f)]. Here, $\lambda = 0.15$, $k_B T = 0.05$, $\Delta t = 0.1$.

optical conductivity observed above the CDW transition in the Falicov-Kimball model, which has been interpreted as an effect of weak localization at small interaction strengths [62].

Finally, Fig. 6 shows $P(\omega)$ for the 2D case before and after the pump is applied. The noninteracting system has a van-Hove singularity at $\omega = 0$ that is split by the Peierls distortion. As already discussed for the 1D case, the occupation of the equilibrium spectrum in Fig. 6(a) is governed by the Fermi-Dirac distribution. Application of the pump field leads to a

broad range of excitations in the upper band, as can be seen in Fig. 6(b). In the CDW phase, we find well-defined peaks in the upper and lower bands which get smeared out as the temperature reaches $k_B T_c \approx 0.1$. While the Peierls gap might disappear in the transient regime, it is recovered once the pulse is over. Furthermore, we find that with increasing $k_B T$ spectral weight transfers towards the upper edge around $\omega = 4.0$. Note that the low-amplitude oscillations in the spectra, especially at high $k_B T$, arise from the statistical fluctuations in the Monte Carlo data; the large-amplitude oscillations in Fig. 6(b) are a real effect.

V. CONCLUSIONS AND OUTLOOK

We have shown that the real-time evolution of electron-phonon models driven by a time-dependent electromagnetic field can be calculated efficiently in the adiabatic limit. To this end, we used a classical Monte Carlo method that samples the equilibrium phonon distribution and combined it with nonequilibrium Green's function techniques. For each Monte Carlo configuration, we solved a noninteracting but time-dependent electronic model with static phonon fields $\vec{q}$ as the phonons lose their dynamics in the adiabatic limit. This simplification allowed us to reach system sizes of 162 sites for a 1D chain and 16×16 sites for the 2D square lattice, which is sufficient to control finite-size effects. We demonstrated that size effects in nonequilibrium observables can be substantially reduced in the presence of a magnetic flux quantum threaded through the square lattice—a common trick in equilibrium Monte Carlo simulations [61]. We presented results for the 1D and 2D Holstein model driven by a time-dependent pump field. For different initial temperatures, we calculated the transient dynamics of the electronic energy and the current as well as the photoemission spectra before and after the pulse. We observed that thermal fluctuations enhance the system's ability to absorb energy from the pump. Moreover, the current is only slightly damped within the CDW
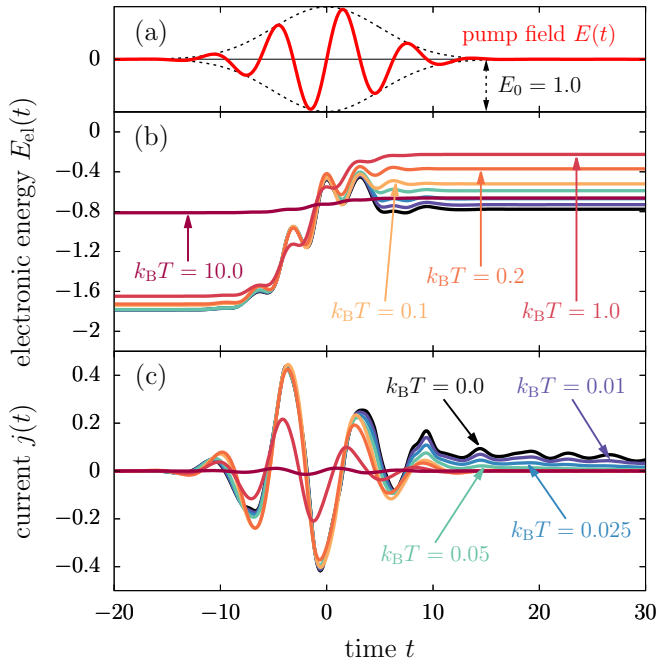

FIG. 5. Time-dependent response of the 2D spinful Holstein model on the square lattice for different initial temperatures. For the pump field shown in panel (a), we plot (b) the electronic energy and (c) the current. Here, $\lambda = 0.15$, $L = 16$, and $\Phi = 1$.
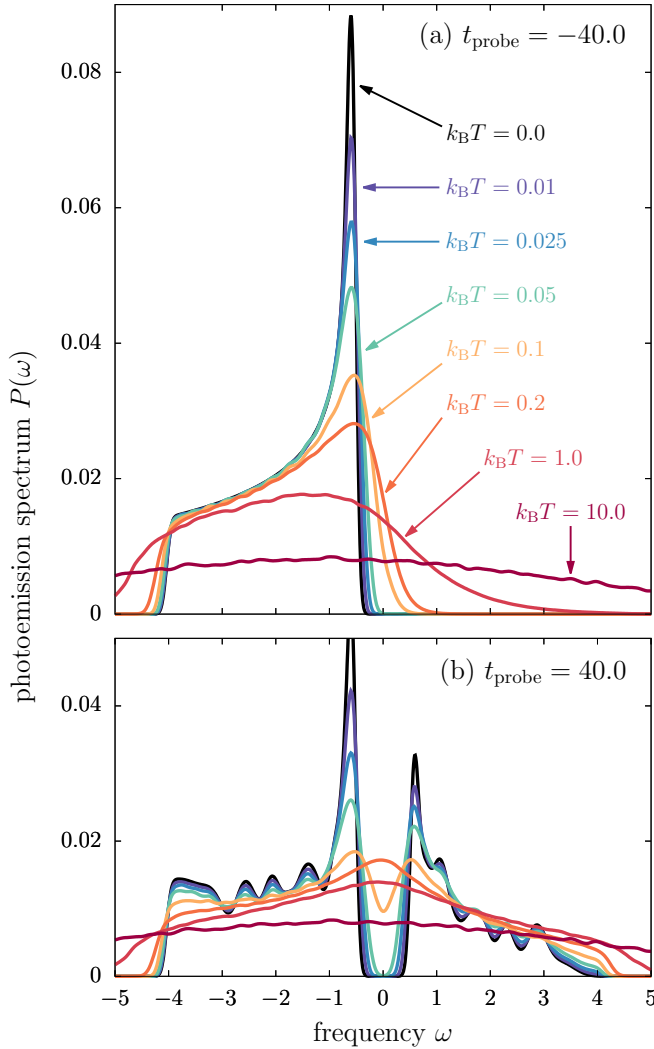
FIG. 6. Photoemission spectrum of the 2D spinful Holstein model on the square lattice (a) before and (b) after the pump for different initial temperatures. Here, $L = 16$, $\lambda = 0.15$, and $\Phi = 1$.

phase of the 2D model, whereas phonon fluctuations lead to a stronger suppression of $j(t)$ in the disordered phase. Finally, we were able to resolve the fine structure in the photoemission spectra which appears in the CDW phase and gets smeared out by thermal fluctuations. All in all, we demonstrated that the classical Monte Carlo approach is well suited for studying driven quantum systems coupled to classical degrees of freedom. The formalism outlined in this paper not only applies to electron-phonon models but also to other types of interactions as they appear, e.g., in the Falicov-Kimball model or the double-exchange model.

The adiabatic limit is expected to be a good approximation for short times after the pump has been applied. In this regime, the electrons can scatter off the thermally induced phonon disorder and relax toward a state with zero current. However, the static phonons prohibit the exchange of energy between electrons and phonons which is crucial for the correct long-time behavior observed in experiments. To include these effects, one has to solve the full quantum phonon problem, which is significantly harder than the adiabatic limit discussed in this paper; indeed, no algorithm is known that will work for large system sizes and long times on these types of problems. For example, exact diagonalization results of the nonequilibrium problem are available on only up to eight lattice sites [13]. A recent DMRG study of the 1D Holstein model driven far from equilibrium reached timescales of $t \approx 6$ on 13 sites [16], whereas larger systems were obtained for a weakly driven system [15]. For both methods, the growing phonon occupation in the unbound bosonic Hilbert space prohibits simulating to longer times. Moreover, DMRG works best at zero temperature and at high phonon frequencies where the separation between the free-phonon energy levels is large [16]. By contrast, the Monte Carlo method discussed in this paper works at $\omega_0 = 0$ and finite temperatures, where larger system sizes and longer times can be obtained. It has the advantage that it is also applicable to 2D where the out-of-equilibrium response can be studied across the finite-temperature Ising transition for these CDW-ordered systems. We expect that our finite-temperature results remain accurate for low phonon frequencies, as long as $k_B T \gg \omega_0$. To obtain a dynamical response of the phonons, it is possible to include an approximate molecular dynamics where the phonons are propagated using their classical equations of motion [63], as has been done for ground-state simulations [11,12,64] and finite distributions for the initial phonon configurations [65,66]. Nonetheless, finite phonon dynamics takes place on timescales proportional to the inverse phonon frequency. If the electronic system is driven out of equilibrium by a short pump pulse, our results obtained in the adiabatic limit will be a good approximation at least until the phonon dynamics sets in.

ACKNOWLEDGMENTS

[1] D. N. Basov, R. D. Averitt, D. van der Marel, M. Dressel, and K. Haule, Electrodynamics of correlated electron materials, Rev. Mod. Phys. **83**, 471 (2011).

[2] L. Perfetti, P. A. Loukakos, M. Lisowski, U. Bovensiepen, H. Berger, S. Biermann, P. S. Cornaglia, A. Georges, and M.

Wolf, Time Evolution of the Electronic Structure of $1T-\text{TaS}_2$ Through the Insulator-Metal Transition, Phys. Rev. Lett. **97**, 067402 (2006).

[3] S. Hellmann, M. Beye, C. Sohrt, T. Rohwer, F. Sorgenfrei, H. Redlin, M. Kalläne, M. Marczynski-Bühlow, F. Hennies, M.

Bauer, A. Föhlisch, L. Kipp, W. Wurth, and K. Rossnagel, Ultrafast Melting of a Charge-Density Wave in the Mott Insulator $1T-TaS_2$, Phys. Rev. Lett. **105**, 187401 (2010).

[4] L. Stojchevska, I. Vaskivskyi, T. Mertelj, P. Kusar, D. Svetin, S. Brazovskii, and D. Mihailovic, Ultrafast switching to a stable hidden quantum state in an electronic crystal, Science **344**, 177 (2014).

[5] T.-R. T. Han, F. Zhou, C. D. Malliakas, P. M. Duxbury, S. D. Mahanti, M. G. Kanatzidis, and C.-Y. Ruan, Exploration of metastability and hidden phases in correlated electron crystals visualized by femtosecond optical doping and electron crystallography, Sci. Adv. **1**, e1400173 (2015).

[6] S. Vogelgesang, G. Storeck, J. G. Horstmann, T. Diekmann, M. Sivis, S. Schramm, K. Rossnagel, S. Schäfer, and C. Ropers, Phase ordering of charge density waves traced by ultrafast low-energy electron diffraction, Nat. Phys. **14**, 184 (2018).

[7] A. Zong, X. Shen, A. Kogar, L. Ye, C. Marks, D. Chowdhury, T. Rohwer, B. Freelon, S. Weathersby, R. Li, J. Yang, J. Checkelsky, X. Wang, and N. Gedik, Ultrafast manipulation of mirror domain walls in a charge density wave, Sci. Adv. **4**, eaau550 (2018).

[8] M. Ligges, I. Avigo, D. Golež, H. U. R. Strand, Y. Beyazit, K. Hanff, F. Diekmann, L. Stojchevska, M. Kalläne, P. Zhou, K. Rossnagel, M. Eckstein, P. Werner, and U. Bovensiepen, Ultrafast Doublon Dynamics in Photoexcited $1T$-TaS_2, Phys. Rev. Lett. **120**, 166401 (2018).

[9] F. Schmitt, P. S. Kirchmann, U. Bovensiepen, R. G. Moore, L. Rettig, M. Krenz, J.-H. Chu, N. Ru, L. Perfetti, D. H. Lu, M. Wolf, I. R. Fisher, and Z.-X. Shen, Transient electronic structure and melting of a charge density wave in TbTe3, Science **321**, 1649 (2008).

[10] F. Zhou, J. Williams, S. Sun, C. D. Malliakas, M. G. Kanatzidis, A. F. Kemper, and C.-Y. Ruan, Nonequilibrium dynamics of spontaneous symmetry breaking into a hidden state of charge-density wave, Nat. Commun. **12**, 566 (2021).

[11] K. Yonemitsu and N. Maeshima, Photoinduced melting of charge order in a quarter-filled electron system coupled with different types of phonons, Phys. Rev. B **76**, 075105 (2007).

[12] S. Miyashita, Y. Tanaka, S. Iwai, and K. Yonemitsu, Charge, lattice, and spin dynamics in photoinduced phase transitions from charge-ordered insulator to metal in quasi-two-dimensional organic conductors, J. Phys. Soc. Jpn. **79**, 034708 (2010).

[13] G. De Filippis, V. Cataudella, E. A. Nowadnick, T. P. Devereaux, A. S. Mishchenko, and N. Nagaosa, Quantum Dynamics of the Hubbard-Holstein Model in Equilibrium and Nonequilibrium: Application to Pump-Probe Phenomena, Phys. Rev. Lett. **109**, 176402 (2012).

[14] H. Matsueda, S. Sota, T. Tohyama, and S. Maekawa, Relaxation dynamics of photocarriers in one-dimensional mott insulators coupled to phonons, J. Phys. Soc. Jpn. **81**, 013701 (2012).

[15] H. Hashimoto and S. Ishihara, Photoinduced charge-order melting dynamics in a one-dimensional interacting Holstein model, Phys. Rev. B **96**, 035154 (2017).

[16] J. Stolpp, J. Herbrych, F. Dorfner, E. Dagotto, and F. Heidrich-Meisner, Charge-density-wave melting in the one-dimensional holstein model, Phys. Rev. B **101**, 035134 (2020).

[17] J. Sous, B. Kloss, D. M. Kennes, D. R. Reichman, and A. J. Millis, Phonon-induced disorder in dynamics of optically pumped metals from nonlinear electron-phonon coupling, Nat. Commun. **12**, 5803 (2021).

[18] M. Weber and M. Hohenadler, Two-dimensional Holstein-Hubbard model: Critical temperature, Ising universality, and bipolaron liquid, Phys. Rev. B **98**, 085405 (2018).

[19] N. C. Costa, K. Seki, S. Yunoki, and S. Sorella, Phase diagram of the two-dimensional Hubbard-Holstein model, Commun. Phys. **3**, 80 (2020).

[20] C. Chen, X. Y. Xu, Z. Y. Meng, and M. Hohenadler, Charge-Density-Wave Transitions of Dirac Fermions Coupled to Phonons, Phys. Rev. Lett. **122**, 077601 (2019).

[21] Y.-X. Zhang, W.-T. Chiu, N. C. Costa, G. G. Batrouni, and R. T. Scalettar, Charge Order in the Holstein Model on a Honeycomb Lattice, Phys. Rev. Lett. **122**, 077602 (2019).

[22] N. C. Costa, K. Seki, and S. Sorella, Magnetism and Charge Order in the Honeycomb Lattice, Phys. Rev. Lett. **126**, 107205 (2021).

[23] B. Cohen-Stead, K. Barros, Z. Meng, C. Chen, R. T. Scalettar, and G. G. Batrouni, Langevin simulations of the half-filled cubic Holstein model, Phys. Rev. B **102**, 161108(R) (2020).

[24] S. Li and S. Johnston, Quantum Monte Carlo study of lattice polarons in the two-dimensional three-orbital Su-Schrieffer-Heeger model, npj Quantum Mater. **5**, 40 (2020).

[25] B. Xing, W.-T. Chiu, D. Poletti, R. T. Scalettar, and G. Batrouni, Quantum Monte Carlo Simulations of the 2D Su-Schrieffer-Heeger Model, Phys. Rev. Lett. **126**, 017601 (2021).

[26] X. Cai, Z.-X. Li, and H. Yao, Antiferromagnetism Induced by Bond Su-Schrieffer-Heeger Electron-Phonon Coupling: A Quantum Monte Carlo Study, Phys. Rev. Lett. **127**, 247203 (2021).

[27] A. Goetz, S. Beyl, M. Hohenadler, and F. F. Assaad, Langevin dynamics simulations of the two-dimensional Su-Schrieffer-Heeger model, arXiv:2102.08899.

[28] M. Weber, Valence bond order in a honeycomb antiferromagnet coupled to quantum phonons, Phys. Rev. B **103**, L041105 (2021).

[29] T. Ohgoe and M. Imada, Competition among Superconducting, Antiferromagnetic, and Charge Orders with Intervention by Phase Separation in the 2D Holstein-Hubbard Model, Phys. Rev. Lett. **119**, 197001 (2017).

[30] S. Karakuzu, L. F. Tocchio, S. Sorella, and F. Becca, Superconductivity, charge-density waves, antiferromagnetism, and phase separation in the Hubbard-Holstein model, Phys. Rev. B **96**, 205145 (2017).

[31] J. K. Freericks, V. M. Turkowski, and V. Zlatić, Nonequilibrium Dynamical Mean-Field Theory, Phys. Rev. Lett. **97**, 266408 (2006).

[32] H. Aoki, N. Tsuji, M. Eckstein, M. Kollar, T. Oka, and P. Werner, Nonequilibrium dynamical mean-field theory and its applications, Rev. Mod. Phys. **86**, 779 (2014).

[33] O. P. Matveev, A. M. Shvaika, T. P. Devereaux, and J. K. Freericks, Nonequilibrium response of an electron-mediated charge density wave ordered material to a large dc electric field, Phys. Rev. B **93**, 045110 (2016).

[34] O. P. Matveev, A. M. Shvaika, T. P. Devereaux, and J. K. Freericks, Time-domain pumping a quantum-critical charge density wave ordered material, Phys. Rev. B **94**, 115167 (2016).

[35] O. P. Matveev, A. M. Shvaika, T. P. Devereaux, and J. K. Freericks, Stroboscopic Tests for Thermalization of Electrons in Pump-Probe Experiments, Phys. Rev. Lett. **122**, 247402 (2019).

[36] P. Werner and M. Eckstein, Phonon-enhanced relaxation and excitation in the Holstein-Hubbard model, Phys. Rev. B **88**, 165108 (2013).

[37] P. Werner and M. Eckstein, Field-induced polaron formation in the Holstein-Hubbard model, Europhys. Lett. **109**, 37002 (2015).

[38] Y. Murakami, P. Werner, N. Tsuji, and H. Aoki, Interaction quench in the Holstein model: Thermalization crossover from electron- to phonon-dominated relaxation, Phys. Rev. B **91**, 045128 (2015).

[39] M. Sentef, A. F. Kemper, B. Moritz, J. K. Freericks, Z.-X. Shen, and T. P. Devereaux, Examining Electron-Boson Coupling Using Time-Resolved Spectroscopy, Phys. Rev. X **3**, 041033 (2013).

[40] A. F. Kemper, M. Sentef, B. Moritz, C. C. Kao, Z. X. Shen, J. K. Freericks, and T. P. Devereaux, Mapping of unoccupied states and relevant bosonic modes via the time-dependent momentum distribution, Phys. Rev. B **87**, 235139 (2013).

[41] A. F. Kemper, M. A. Sentef, B. Moritz, J. K. Freericks, and T. P. Devereaux, Effect of dynamical spectral weight redistribution on effective interactions in time-resolved spectroscopy, Phys. Rev. B **90**, 075126 (2014).

[42] K. Michielsen and H. De Raedt, Quantum molecular dynamics study of the Su-Schrieffer-Heeger model, Z. Phys. B **103**, 391 (1997).

[43] K. Michielsen and H. D. Raedt, Optical absorption in the soliton model for polyacetylene, Mod. Phys. Lett. B **10**, 467 (1996).

[44] S. Yunoki, J. Hu, A. L. Malvezzi, A. Moreo, N. Furukawa, and E. Dagotto, Phase Separation in Electronic Models for Manganites, Phys. Rev. Lett. **80**, 845 (1998).

[45] J.-P. Pouget, The Peierls instability and charge density wave in one-dimensional electronic conductors, C. R. Phys. **17**, 332 (2016).

[46] B. Guster, M. Pruneda, P. Ordejón, E. Canadell, and J.-P. Pouget, Evidence for the weak coupling scenario of the Peierls transition in the blue bronze, Phys. Rev. Materials **3**, 055001 (2019).

[47] S. A. Brazovskii and I. E. Dzyaloshinskii, Dynamics of a one-dimensional electron-phonon system at low temperatures, Zh. Eksp. Teor. Fiz. **71**, 2338 (1976).

[48] M. Weber, F. F. Assaad, and M. Hohenadler, Thermal and quantum lattice fluctuations in Peierls chains, Phys. Rev. B **98**, 235117 (2018).

[49] T. Holstein, Studies of polaron motion: Part I. The molecular-crystal model, Ann. Phys. **8**, 325 (1959).

[50] M. Weber, F. F. Assaad, and M. Hohenadler, Thermodynamic and spectral properties of adiabatic Peierls chains, Phys. Rev. B **94**, 155150 (2016).

[51] K. Michielsen, H. De Raedt, and T. Schneider, Metal-Insulator Transition in a Generalized Hubbard Model, Phys. Rev. Lett. **68**, 1410 (1992).

[52] M. M. Maśka and K. Czajka, Thermodynamics of the two-dimensional Falicov-Kimball model: A classical Monte Carlo study, Phys. Rev. B **74**, 035109 (2006).

[53] J. Nasu, M. Udagawa, and Y. Motome, Vaporization of Kitaev Spin Liquids, Phys. Rev. Lett. **113**, 197205 (2014).

[54] K. Hukushima and K. Nemoto, Exchange Monte Carlo Method and Application to Spin Glass Simulations, J. Phys. Soc. Jpn. **65**, 1604 (1996).

[55] M. Žonda and M. Thoss, Nonequilibrium charge transport through Falicov-Kimball structures connected to metallic leads, Phys. Rev. B **99**, 155157 (2019).

[56] A. J. Herrmann, A. E. Antipov, and P. Werner, Spreading of correlations in the Falicov-Kimball model, Phys. Rev. B **97**, 165107 (2018).

[57] M. Weber and J. K. Freericks, Field Tuning Beyond the Heat Death of a Charge-Density-Wave Chain, arXiv:2107.04096.

[58] J. K. Freericks, H. R. Krishnamurthy, and T. Pruschke, Theoretical Description of Time-Resolved Photoemission Spectroscopy: Application to Pump-Probe Experiments, Phys. Rev. Lett. **102**, 136401 (2009).

[59] See Supplemental Material at http://link.aps.org/supplemental/10.1103/PhysRevE.105.025301 for the data files for the results presented in this paper.

[60] W. Shen, T. P. Devereaux, and J. K. Freericks, Exact solution for Bloch oscillations of a simple charge-density-wave insulator, Phys. Rev. B **89**, 235129 (2014).

[61] F. F. Assaad, Depleted Kondo lattices: Quantum Monte Carlo and mean-field calculations, Phys. Rev. B **65**, 115104 (2002).

[62] A. E. Antipov, Y. Javanmard, P. Ribeiro, and S. Kirchner, Interaction-Tuned Anderson Versus Mott Localization, Phys. Rev. Lett. **117**, 146601 (2016).

[63] M. D. Petrović, M. Weber, J. K. Freericks (unpublished).

[64] K. Iwano, Mechanism for photoinduced structural phase transitions in low-dimensional electron-lattice systems: Nonlinearity with respect to excitation density and aggregation of excited domains, Phys. Rev. B **61**, 279 (2000).

[65] A. Troisi and G. Orlandi, Charge-Transport Regime of Crystalline Organic Semiconductors: Diffusion Limited by Thermal Off-Diagonal Electronic Disorder, Phys. Rev. Lett. **96**, 086601 (2006).

[66] J. H. Fetherolf, D. Golež, and T. C. Berkelbach, A Unification of the Holstein Polaron and Dynamic Disorder Pictures of Charge Transport in Organic Crystals, Phys. Rev. X **10**, 021062 (2020).

[67] www.gauss-centre.eu.

[68] www.lrz.de.